

The polar mesospheric cloud mass in the Arctic summer

Michael H. Stevens and Christoph R. Englert

E.O. Hulburt Center for Space Research, Washington, D. C., USA

Matthew T. DeLand

Science Systems and Applications, Inc., Lanham, Maryland, USA

Mark Hervig

G & A Technical Software, Inc., Driggs, Idaho, USA

Received 28 April 2004; revised 15 November 2004; accepted 21 December 2004; published 19 February 2005.

[1] We infer the polar mesospheric cloud (PMC) mass throughout the Arctic summer using results from two sets of satellite observations and a microphysical model. Solar backscatter ultraviolet (SBUV) PMC observations in July 1999 indicate a burst of activity persisting for ~ 8 days after a space shuttle launch and averaging 262 ± 52 t near 4.7 local time. This mass is consistent with the propellant mass available from the shuttle's main engines and accounts for 22% of the total SBUV PMC mass over the season between 65° and 75°N . This is the first evidence that PMCs formed by space shuttle water exhaust can contribute significantly to both the number of observed PMCs and the total PMC mass in a season. In another approach, 11 years of observations by the Halogen Occultation Experiment (HALOE) indicate that on average 90 ± 12 t of water ice is present near local midnight between 65° and 75°N . Using simultaneous HALOE water vapor observations, we find that a one-dimensional microphysical model reproduces the start and end of the PMC season but overpredicts the ice mass by about a factor of 1.8 when compared with the observations. This overprediction is within the time-dependent variability of ice formation and the uncertainties of temperature, water vapor, and vertical winds used to initialize the model.

Citation: Stevens, M. H., C. R. Englert, M. T. DeLand, and M. Hervig (2005), The polar mesospheric cloud mass in the Arctic summer, *J. Geophys. Res.*, 110, A02306, doi:10.1029/2004JA010566.

1. Introduction

[2] Since the 1880s, mesospheric clouds have fascinated skywatchers with occasionally brilliant displays [Leslie, 1885]. Interest renewed in the 1970s [Donahue *et al.*, 1972] when their population around the entire summer pole was documented using satellite data. Although many describe their appearance, the processes leading to their formation and controlling their observed variability are still both uncertain and disputed.

[3] Normally appearing near 82 km at high latitudes in the summer, some argue that these polar mesospheric clouds (PMCs) respond to anthropogenic forcing from the lower atmosphere [e.g., Thomas *et al.*, 1989; Thomas and Olivero, 2001]. To this end, both the PMC frequency and the brightness have been studied separately in search of long-term (>10 years) and short-term changes [e.g., von Zahn *et al.*, 2004; Kirkwood and Stebel, 2003; von Zahn, 2003; Thomas *et al.*, 2003].

[4] This work presents analyses of two PMC data sets obtained during northern summers. Rather than treat the

PMC frequency and brightness (or extinction) separately, we herein combine them into one quantity. This quantity is the zonally integrated ice mass, which does not require clarification of viewing conditions, lighting conditions, or wavelength. We define the PMC ice mass as the total mass detected from satellite observations of PMCs and the mesospheric ice mass as the total mass of all mesospheric ice particles, including subvisible particles. To our knowledge this is the first study to calculate either of these quantities in a zonally integrated sense.

[5] One way to infer the PMC mass is from UV scattered sunlight observed by the solar backscatter ultraviolet (SBUV) experiment. Various SBUV instruments have observed PMCs every year in both hemispheres since 1979. These data are routinely reported as cloud frequency and albedo throughout a PMC season [Thomas *et al.*, 1991; DeLand *et al.*, 2003]. With an assumption about the ice particle size distribution these can yield the PMC ice mass on any given day.

[6] By inferring the zonally averaged PMC ice mass from the SBUV observations, we also consider the possibility that this mass is significantly increased by water vapor exhaust from the main engines of the space shuttle. Recent work showed that lower thermospheric transport of a shuttle

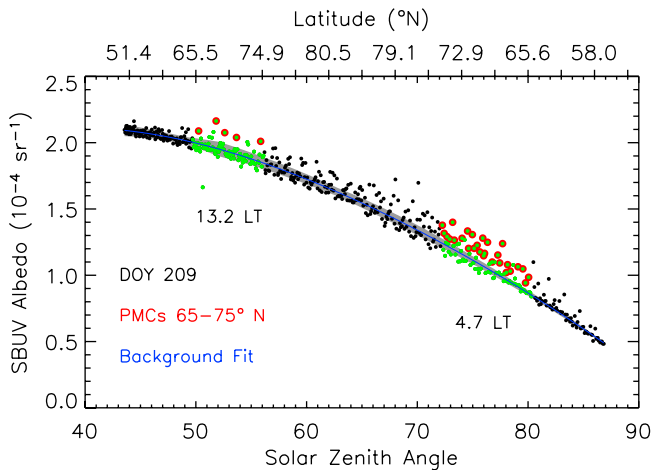


Figure 1. SBUV albedo at 252 nm measured from the NOAA 14 satellite on 28 July 1999 (day of year (DOY) 209). Green symbols are observations between 65° and 75°N, and highlighted red symbols indicate identified PMCs in this latitude region. Shaded area represents the threshold beyond which a PMC may be inferred. Not all points exceeding the threshold are identified as PMCs due to other tests used [DeLand *et al.*, 2003].

exhaust plume to the Arctic can produce PMCs [Stevens *et al.*, 2003], but an estimation of its relative contribution to a season of PMC observations has not yet been made. PMCs are confined to summertime high latitudes and sequester on average only 2–4 ppmv of water vapor over ~4 km altitude [Hervig *et al.*, 2003]. Therefore, although launch vehicle exhaust cannot appreciably contribute to the global mesospheric water vapor budget [Turco *et al.*, 1982], PMCs represent a much smaller reservoir, which is far more sensitive to the effects of space vehicle exhaust. If this exhaust routinely reaches the Arctic from as far away as the subtropics, it could bias late twentieth century PMC observations and obscure the role of PMCs as indicators of climate change from below.

[7] Another way to determine the PMC mass is to use observations from the Halogen Occultation Experiment (HALOE) on NASA's Upper Atmospheric Research Satellite. HALOE observations include vertical profiles of PMCs and water vapor in the Arctic summer mesosphere since 1992. HALOE measures ice particle extinction in the infrared at five different wavelengths from 2.45 to 6.26 μm [McHugh *et al.*, 2003]. These are reported in frequency and average extinction from which the equivalent water vapor content and the PMC mass can be inferred. The HALOE PMC observations are useful because they are a direct measure of the ice volume along the line of sight and therefore do not require assumptions about the particle size distribution to infer the PMC ice mass.

[8] A more theoretical approach is to use HALOE Arctic summer water vapor observations as input to a microphysical model to predict the water expected in the ice phase. Recently, Hervig *et al.* [2003] reported HALOE water vapor observations averaged over a solar cycle in the Arctic summer mesosphere. The reprocessed data between April

and October are distinguished by a surprisingly large summertime water vapor layer near PMCs [Summers *et al.*, 2001], which peaks at ~8 ppmv. These unique observations can be used to initialize a cloud formation model and predict the onset, the peak, and the demise of mesospheric clouds over a typical Arctic summer for comparison against observations. By estimating the contribution of ice particles undetected by HALOE, the total (mesospheric) ice mass can then be directly compared against the prediction.

[9] This work has three objectives: (1) infer the PMC mass from SBUV observations at mid solar cycle over one northern summer, (2) determine whether water vapor exhaust from one space shuttle launch can contribute significantly to a season of (SBUV) PMC observations, and (3) use HALOE water vapor observations of the Arctic summer mesosphere in a microphysical model to predict the mesospheric ice mass and compare with HALOE PMC observations.

2. SBUV PMC Observations

2.1. Data Analysis

[10] Since 1979 the SBUV instruments have observed the Earth's ultraviolet albedo in the nadir from an altitude of 850 km. Although designed to measure ozone, the instruments also observe PMCs up to 81° latitude during the summer months [Thomas *et al.*, 1991]. By estimating and subtracting the background solar scattered light, the PMC albedo can be inferred at five different wavelengths between 252 and 292 nm.

[11] We focus on NOAA 14 observations of the 1999 Northern Hemisphere summer about halfway between a minimum and a maximum of the solar cycle. We consider data between 65° and 75°N latitudes, which comprises 44% of the Earth's area poleward of 60°N. This region is chosen because it includes latitudes where HALOE also measured PMCs (65°–70°N) and it is where both water vapor and temperature observations are available for modeling PMC formation (section 3). The SBUV cloud detection algorithm is described by DeLand *et al.* [2003] with two improvements described below.

[12] The SBUV albedo is defined as the nadir-viewing radiance divided by the solar irradiance and is shown for a day of observations (28 July or day of year 209) during the polar summer in Figure 1. The gradual reduction in the albedo with increasing solar zenith angle (SZA) is primarily due to increased attenuation of the 252-nm flux in the lower mesosphere by ozone, which results in less Rayleigh scattered light reaching the instrument. DeLand *et al.* [2003] estimated the background albedo with a fourth-order polynomial in an algorithm that identified and removed PMCs iteratively and recalculated the background albedo after each iteration. The brightness of each cloud was referenced to the iteration in which it was identified. In the present analysis the brightness is referenced to the background calculated in the final iteration (blue curve), which is a better estimate of the Earth's clear air albedo. The second improvement is that a 5- σ threshold is imposed on the backscattered albedo observations, which prevents negative and positive outliers from biasing the polynomial fit and leading to spurious detections. A 1- σ threshold is shown as the

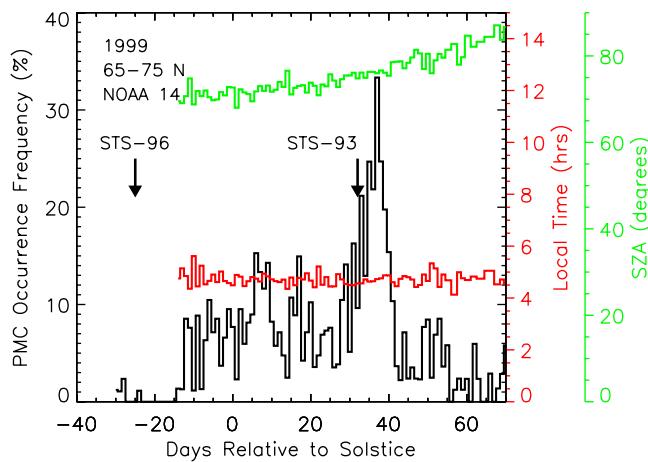


Figure 2. PMC occurrence frequency for the 1999 Northern Hemisphere summer near 4.7 local time. The variation of local time and solar zenith angle (averaged over the indicated latitudes) are shown as the red curve and the green curve, respectively. The dates of the two shuttle launches within this time period are also shown by their designations (STS 96 and STS 93).

shaded region in Figure 1. For the NOAA 14 Northern Hemisphere 1999 data considered here, these two improvements uniformly increase the inferred PMC albedo for each day by approximately 3–18%. The PMC albedo change averaged over the entire season is +10% (M. T. DeLand et al., A quarter century of satellite PMC observations, submitted to *Journal of Atmospheric and Solar-Terrestrial Physics*, 2004).

[13] Figure 1 also serves to illustrate that between 65° and 75°N, SBUV observes PMCs (highlighted in red) near 13.2 local time (LT) on the ascending node of the orbit and near 4.7 LT on the descending node. Note that there are far more PMCs observed at 4.7 LT than at 13.2 LT, even though the same latitudes and longitudes were sampled on the same day. This is evidence of a local time dependence on the cloud frequency with an early morning bias. We will leave a complete local time analysis of SBUV PMCs for future work. From this point on we only consider the observations on the descending node near 4.7 local time.

[14] The PMC occurrence frequency as inferred from SBUV observations is plotted against days relative to solstice (DRS) in Figure 2. The relatively small variation of local time (in red) and solar zenith angle (in green) for these observations is also shown for reference. The dates of two space shuttle launches are indicated, and there is dramatically enhanced PMC activity following launch of STS 93 on 23 July 1999. Figure 3 shows the inferred PMC albedos against DRS as the black histogram. There is a slight enhancement to the albedo following launch of STS 93 that is resonant with the frequency enhancement in Figure 2. This could be related to ice formation from shuttle water vapor exhaust, but the variability of the albedo throughout the season makes identification of the cause ambiguous. Nonetheless, the combination of the increased occurrence frequency near 37 DRS and the albedo enhance-

ment produce an unambiguous increase in the PMC mass, as will be shown next.

2.2. PMC Mass

[15] Our interpretation of cloud albedo uses standard Mie theory [Bohren and Huffman, 1983], which requires an assumption about the ice particle size distribution. We assume a lognormal distribution with a median radius of 55 nm and a distribution width of 1.42, consistent with the ground-based mesospheric cloud observations by von Cossart et al. [1999].

[16] In general, the spectral radiance L (in $\text{erg cm}^{-2} \text{s}^{-1} \text{nm}^{-1} \text{sr}^{-1}$) scattered into the SBUV field of view by a PMC can be calculated using

$$L(N_C, \theta, \lambda) = N_C \Phi_{S,\lambda} \Sigma_i [q(\theta, \lambda, r_i) \pi r_i^2 n(r_i)], \quad (1)$$

where N_C is the PMC ice particle column number density (in cm^{-2}), θ is the scattering angle, λ is the wavelength (in this case 252 nm), $q(\theta, \lambda, r_i)$ (in sr^{-1}) is the scattering intensity coefficient, $\Phi_{S,\lambda}$ is the spectral solar irradiance (in $\text{erg cm}^{-2} \text{s}^{-1} \text{nm}^{-1}$), r_i is the particle radius, and $n(r_i)$ is the normalized particle density. In the SBUV nadir-viewing geometry, the scattering angle θ is the supplement of the solar zenith angle (i.e., $180^\circ - \text{SZA} = \theta$). For the calculation of $q(\theta, \lambda, r_i)$ we use an ice refractive index of 1.3509 [Warren, 1984].

[17] The radiance from a PMC as measured by SBUV can also be calculated using the SBUV albedo definition:

$$L_{\theta,\lambda} = \Phi_{S,\lambda} A_{\theta,\lambda}, \quad (2)$$

where $L_{\theta,\lambda}$ is the cloud radiance measured by SBUV and $A_{\theta,\lambda}$ is the SBUV cloud albedo (in sr^{-1}). We note here that previous work using SBUV PMC data has reported $A_{\theta,\lambda}$ as a

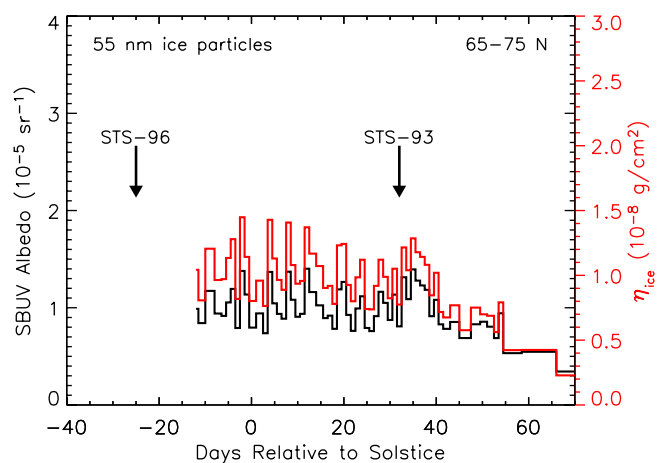


Figure 3. Daily averaged 252-nm albedo of PMCs identified by SBUV (in black) for the same PMC observations in Figure 2. Also shown is the calculated water ice mass column, η_{ice} (in red) for a lognormal distribution using a width parameter of 1.42 and a mean radius of 55 nm [von Cossart et al., 1999].

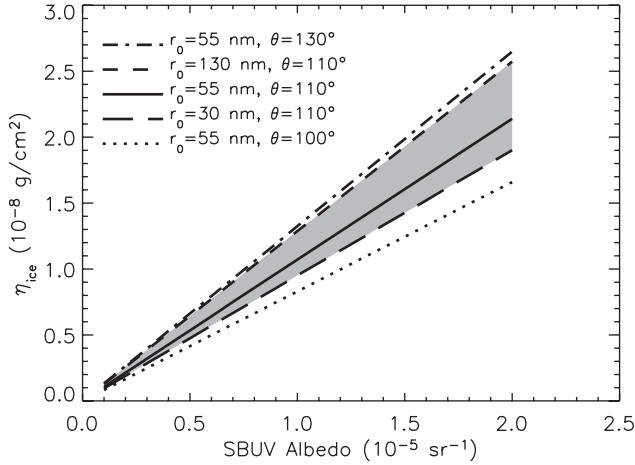


Figure 4. Relationship between the 252-nm albedo and the vertical water ice mass column, η_{ice} . Results for a variety of median radii and typical SBUV scattering angles are shown. The shaded area represents the uncertainty in the water column ($\pm 17\%$) derived from the uncertainty in the ice particle size. The distribution width for these simulations is 1.42.

unitless quantity [e.g., *Thomas et al.*, 1991; *DeLand et al.*, 2003; *Thomas et al.*, 2003].

[18] Equating $L_{\theta,\lambda}$ with $L(N_C, \theta, \lambda)$ yields the PMC ice particle column density:

$$N_C(A_{\theta,\lambda}) = \frac{A_{\theta,\lambda}}{\sum_i [q(\theta, \lambda, r_i) \pi r_i^2 n(r_i)]}. \quad (3)$$

Note that this vertical column of water ice [*Thomas and McKay*, 1985] is independent of the spectral solar irradiance. Using the particle distribution we can calculate the mass column density of water ice η_{ice} (in g cm^{-2}) by

$$\eta_{\text{ice}}(A_{\theta,\lambda}) = \rho(\text{ice}) N_C(A_{\theta,\lambda}) \sum_i [n(r_i) 4\pi r_i^3 / 3]. \quad (4)$$

We model the lognormal distribution in 2-nm bins (i) from 2 to 600 nm and use an ice density of 0.932 g cm^{-3} [*Gadsden*, 1982].

[19] Figure 4 shows the inferred mass column density of water ice for SBUV cloud albedos at 252 nm. The relationship is linear due to the assumption that PMCs are optically thin in the nadir near 252 nm [*Debrestian et al.*, 1997]. We show the dependence on a range of particle radii as well as on the range of scattering angles that are typically observed by SBUV at high latitudes. Describing the ice particle distribution using a Gaussian with the same full width at half maximum as the lognormal distribution yields a water mass column that is within 10% of the lognormal result for the radii and scattering angles of Figure 4. The daily averaged value of η_{ice} as calculated from equation (4) is overplotted on the SBUV albedo in Figure 3 in red and referenced to the right-hand axis.

[20] The equivalent water vapor mixing ratio contained in PMCs, $\text{H}_2\text{O}(\text{ice})$, can be derived from η_{ice} by

$$\text{H}_2\text{O}(\text{ice}) = \frac{\eta_{\text{ice}}(A_{\theta,\lambda})}{\{18u[M]dz\}}, \quad (5)$$

where $18u$ is the mass of a water molecule (in grams), dz is the vertical cloud thickness (in centimeters), and $[M]$ is the ambient number density, which we take to be $4.15 \times 10^{14} \text{ cm}^{-3}$ at a cloud height of 82 km [*Lübken*, 1999]. Using equation (5) and a cloud thickness of 1.0 km, the average $\text{H}_2\text{O}(\text{ice})$ is generally between 5 and 10 ppmv. This is larger than the 2–4 ppmv reported by *Hervig et al.* [2003] using HALOE observations, but the HALOE data have a vertical resolution of 1.5 km for a single scan, and hundreds of scans are averaged over a solar cycle, further reducing the vertical resolution and the reported peak value.

[21] We can also use η_{ice} to estimate the daily averaged PMC ice mass, $I_M(t)$, by

$$I_M(t) = \omega(t) \eta_{\text{ice}}(t) S, \quad (6)$$

where $\omega(t)$ is the daily PMC frequency as given in Figure 2 and S is the area of the 82-km pressure surface between 65° and 75°N ($1.6 \times 10^{17} \text{ cm}^2$). Since SBUV samples all longitudes in one day for the descending (or ascending) node of the orbits, $\omega(t)$ is equivalently the zonally averaged fraction of area S in which there is a cloud. Note that $I_M(t)$ is independent of any assumptions on cloud thickness. $I_M(t)$ determined from the SBUV occurrence frequencies and cloud albedos in Figures 2 and 3 is shown in Figure 5. Between -21 and 59 DRS (31 May to 19 August) the average SBUV PMC ice mass is $136 \pm 27 \text{ t}$.

[22] Varying the median radius from a typical value of 55 nm to reported values which range between 30 and 130 nm [*von Cossart et al.*, 1999; *Hervig et al.*, 2001] yields variations for the equivalent water vapor from our nominal result by $\pm 17\%$. We have no direct information

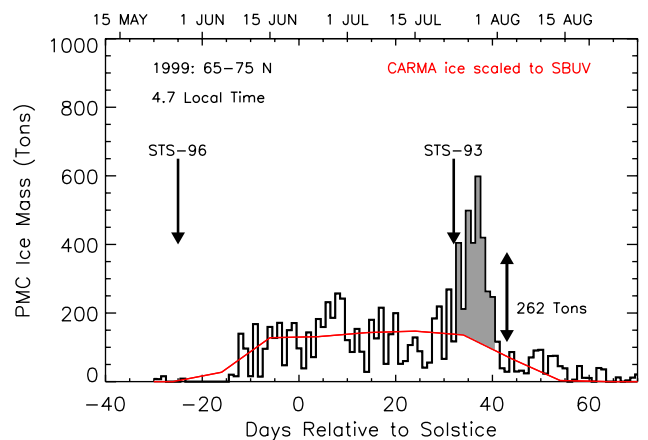


Figure 5. Daily mesospheric ice mass in metric tons for the latitudes indicated. The black histogram is the SBUV data, and the red curve is the CARMA result normalized to the (unshaded) SBUV data. The indicated “excess” ice mass of 262 t is calculated from the 8-day average of the shaded area and is generally consistent with the amount of water vapor injected into the lower thermosphere by the main engines of STS 93.

on the day-to-day variability of particle sizes, so we carry this as an uncertainty to the inferred daily ice mass. Contributions to the total 20% uncertainty are therefore $\pm 17\%$ for the ice particle size and $\pm 10\%$ for the cloud albedo. The red curve in Figure 5 is a scaled model result for the ice mass, which is used to determine the enhanced mass following launch of STS 93 in late July 1999. The model result is discussed further in section 3, and the shuttle contribution is discussed next.

2.3. Shuttle Contribution to the PMC Mass

[23] STS 93 was launched from the Kennedy Space Center on 23 July 1999 near the middle of the PMC season. Roughly half of the water vapor exhaust from the main engines is injected near 110 km off the east coast of the United States [Stevens *et al.*, 2002]. An increase in the Arctic ice mass is clearly evident in Figure 5 starting at 33 DRS, 1 day after launch. Previous work has shown that main engine water vapor exhaust injected near 110 km in the subtropics can be rapidly transported northward to the Arctic in 1–2 days to form PMCs. Indeed Arctic ground-based water vapor observations at 66°N reveal passage of the STS 93 water vapor plume 1.7 days after launch [Hartogh and Song, 2004]. The PMCs formed from the shuttle exhaust ultimately settle to the 82-km region where mean meridional winds move them southward [Stevens *et al.*, 2003]. Figure 5 suggests that these PMCs contributed substantially to the SBUV PMC observations in the 1999 northern summer.

[24] We explore this further by comparing the increase in PMC mass with the propellant mass available. We have scaled the model curve calculated in section 3 to the data in Figure 5 using the portion of the data away from the burst of cloudiness. The indicated 8-day average excess is 262 ± 52 tons, which is $\sim 70\%$ of what is injected by the main engines above 90 km. This is about twice the amount reported sequestered in a burst of PMCs between 6.0 and 7.2 days after the STS 85 launch of 123 ± 62 tons [Stevens *et al.*, 2003], determined from PMC infrared thermal emission. Note, however, that these STS 85 observations were limited to latitudes equatorward of 72°N, whereas the data shown in Figure 5 reach to 75°N. The SBUV data in Figure 5 are therefore quantitative evidence that the enhanced activity following launch of STS 93 is due to water vapor exhaust from the shuttle's main engines that was transported to the Arctic.

[25] What is perhaps most significant about the enhanced mass in Figure 5 is its persistence. Though the observed cloud mass peaks 5 days after launch, there is enhanced PMC activity virtually without interruption between 1 and 8 days after launch, compounding the contribution to the total PMC ice mass. This duration of activity is in reasonable agreement with prevailing southward transport, which moves PMCs over 10° in latitude in ~ 2 –5 days as will be discussed in section 3.2. Note also that the formation of PMCs from a shuttle plume may also take place over a period of days, thereby prolonging the effect on the PMC observations.

[26] From the shaded region in Figure 5 we calculate the relative contribution of STS 93 main engine exhaust clouds to be 22% of the total for the season. This presumes that all PMCs used in Figure 5 can be

represented with the same particle size distribution. This contribution does not include those from other shuttle or rocket launches, which is estimated in section 4.

3. Community Aerosol and Radiation Model for Atmospheres (CARMA)

3.1. Description

[27] The one-dimensional microphysical model used in this work is CARMA. This model takes as input vertical profiles of temperature, water vapor, and vertical winds and calculates the particle growth, sedimentation, and sublimation of ice particles as a function of time for the specified initial conditions. The model includes all known processes relevant to ice formation in the mesosphere and is described in detail by Rapp *et al.* [2002]. The one-dimensional version of CARMA used in this work is the same as that used by Rapp *et al.* with the following modifications:

[28] 1. We incorporate new measurements of water ice vapor pressures extrapolated from lower temperatures (165 K) reported by Mauersberger and Krankowsky [2003].

[29] 2. We initialize the model using HALOE measurements of water vapor in the Arctic summer mesosphere from Hervig *et al.* [2003].

[30] 3. We use vertical winds from a two-dimensional global-scale model (CHEM2D) that peak near 6 cm s^{-1} at 86 km at solstice [Siskind *et al.*, 2005]. This is about twice that used by Rapp *et al.* [Körner and Sonnemann, 2001] but consistent with vertical winds recently reported near summer solstice and 70°N by Berger and von Zahn [2002].

[31] 4. The radius grid used to describe the size distribution of ice particles is herein extended so that the maximum particle size increases from 86 to 412 nm. This ensures that all the larger particles resulting from the greater water vapor abundances and the more vigorous vertical upwelling are modeled.

[32] We specify the Arctic temperatures and ambient densities in CARMA with the climatology from Lübken [1999], which is from ground-based falling sphere observations near 69°N. CARMA results include the time-dependent vertical distribution of water vapor and water ice at high vertical resolution (250 m). We assume that the temperature climatology compiled from observations at 69°N and the zonally averaged HALOE water vapor observations between 65° and 70°N can be used together to predict the average Arctic ice mass between 65° and 75°N. The falling sphere temperatures and the CHEM2D vertical winds are interpolated onto the same time and altitude grid as the zonally averaged water vapor observations. The vertical profiles of water vapor are compiled in 10-day increments throughout the Arctic summer and are set to zero above 86 km where the HALOE data appear unreliable [Hervig *et al.*, 2003]. We find that the contribution of the reported HALOE water vapor between 86 and 88 km to the mesospheric ice mass is only $\sim 3\%$ after freeze-drying of the upper mesosphere, discussed next.

3.2. PMC Simulations

[33] Figure 6 shows time-altitude results of water vapor for 5 July or day of year (DOY) 186. We choose a 4-day simulation under the assumption that the PMC lifetime is predominantly controlled by the mean southward wind near

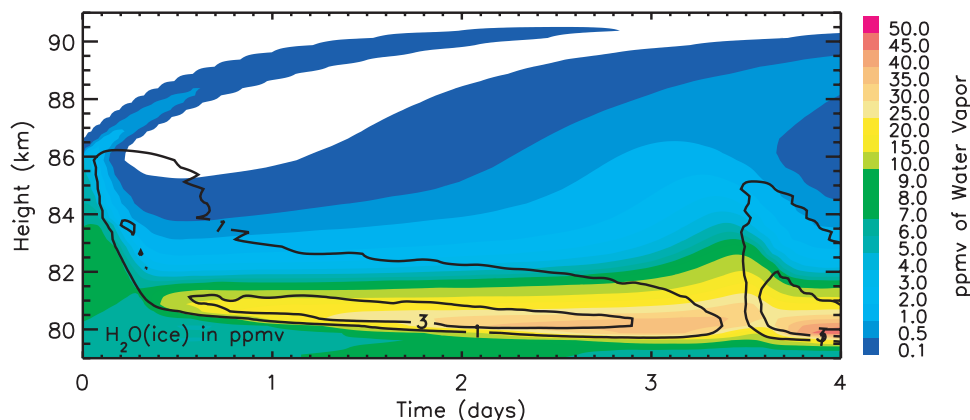


Figure 6. Calculated variation of water vapor and $\text{H}_2\text{O}(\text{ice})$ for 5 July. HALOE water vapor initializes the model and is allowed to form ice, sediment, and sublimate so that the 82-km layer becomes narrower and more concentrated. This narrow layer would not be fully resolved by HALOE (see text).

82 km, which eventually moves PMCs to regions of higher temperatures where they sublimate. Reported mean southward winds near 70°N at these altitudes are $3\text{--}5\text{ m s}^{-1}$ in July [Lieberman *et al.*, 2000; Berger and von Zahn, 2002], which transport PMCs over 10° latitude in $\sim 2\text{--}5$ days. Temperature and vertical winds are kept fixed during the simulation, whereas the water vapor is allowed to vary from the initial condition specified by HALOE. The evolution of water vapor is shown as the colored contours with $\text{H}_2\text{O}(\text{ice})$ overplotted as solid black contours (in ppmv).

[34] Figure 6 serves to illustrate that ice forms near 85 km where the particles grow and fall to the 81-km region. Here they are sustained by low temperatures and vigorous upwelling over the summer pole as found in work using earlier versions of this same model [e.g., Jensen and Thomas, 1988]. Note that the competition between the vertical wind and ice particle sedimentation gives rise to substantial variability of $\text{H}_2\text{O}(\text{ice})$ over the 4-day simulation.

[35] Initially, the water vapor layer near 81 km is 7–8 ppmv, but it becomes even larger during the freeze-drying process. Mixing ratios can occasionally exceed 40 ppmv, which is ~ 5 times greater than the initial condition. This water vapor layer is narrow (~ 1 km), however, and varies slightly in altitude so that the peak will be reduced when time averaging the model output, discussed next.

[36] Figures 7a–7c show CARMA model results throughout the PMC season. CARMA is initialized every 10 days with HALOE water vapor observations as well as the temperature profile and vertical winds interpolated to the HALOE dates (DOY 116–256). Each CARMA simulation is run for 4 days where the averages over days 1–4 are calculated and interpolated over the season. Figure 7a shows the seasonal evolution of vertical winds [Siskind *et al.*, 2005], which sustains the ice particles near 82 km and is held fixed throughout each simulation. Figure 7b shows the degree of water ice supersaturation, and Figure 7c shows the vertically redistributed water vapor.

[37] In general, ice particles can exist when the water vapor partial pressure (p_w) is greater than the saturation pressure of water over ice (p_s) [Thomas, 1991]. This water vapor supersaturation ($S = p_w/p_s$) is often used to specify the region of the atmosphere suitable for particle growth [e.g., Lübken, 1999; Stevens *et al.*, 2001]. Figure 7b illustrates

that $S > 1$ below 83 km from late May to mid-August, generally consistent with observations of mesospheric clouds between 65° and 75°N [Thomas and Olivero, 1989; Fiedler *et al.*, 2003; Hervig *et al.*, 2003]. Figure 7c shows the vertically redistributed water vapor, where the time averaging has degraded the vertical resolution of the 82-km layer so that the modeled peak is ~ 30 ppmv. We add that the water vapor layer in Figure 7c would not be fully resolved in the satellite data. Convolution of the individual retrieved profiles with the HALOE weighting function that has a width of ~ 1.5 km typically reduces the peak of the layer by an additional $\sim 30\%$ to ~ 20 ppmv, still higher than the reported peak of ~ 8 ppmv. We do not herein consider local time effects on the modeled layer, which may additionally limit the comparison of the redistributed water vapor to the heavily averaged HALOE data.

[38] The remainder of section 3 addresses the calculated $\text{H}_2\text{O}(\text{ice})$, which is overplotted as the black contours in Figures 7a–7c. We compare these model results using the HALOE water vapor with the HALOE PMC data and estimate the undetectable ice particles for direct comparison with the predicted mesospheric ice mass.

3.3. Comparison of Results to HALOE PMC Data

[39] The modeled $\text{H}_2\text{O}(\text{ice})$ in Figure 7 was vertically integrated and multiplied by the area between 65° and 75°N latitude to obtain the zonally averaged ice mass shown as the solid line in Figure 8. We scaled the model curve in Figure 8 to the SBUV PMC data in Figure 5 to establish a background and to help quantify enhanced cloud activity following launch of a space shuttle, as discussed in section 2.3. For each 10-day increment we calculate the minimum and maximum ice mass during the simulation, and this is indicated as the shaded area. Unlike the observations, the modeled ice mass in Figure 8 does not require consideration of cloud frequency or detection thresholds.

[40] The $\text{H}_2\text{O}(\text{ice})$ reported by Hervig *et al.* [2003] from observations between 65° and 70°N was also vertically integrated and multiplied by the area between 65° and 75°N . This result is shown in Figure 8 as the long-dashed line. The peak mass inferred from HALOE $\text{H}_2\text{O}(\text{ice})$ is much greater than the model for the start and end of the season. This is because the HALOE extinctions are reported

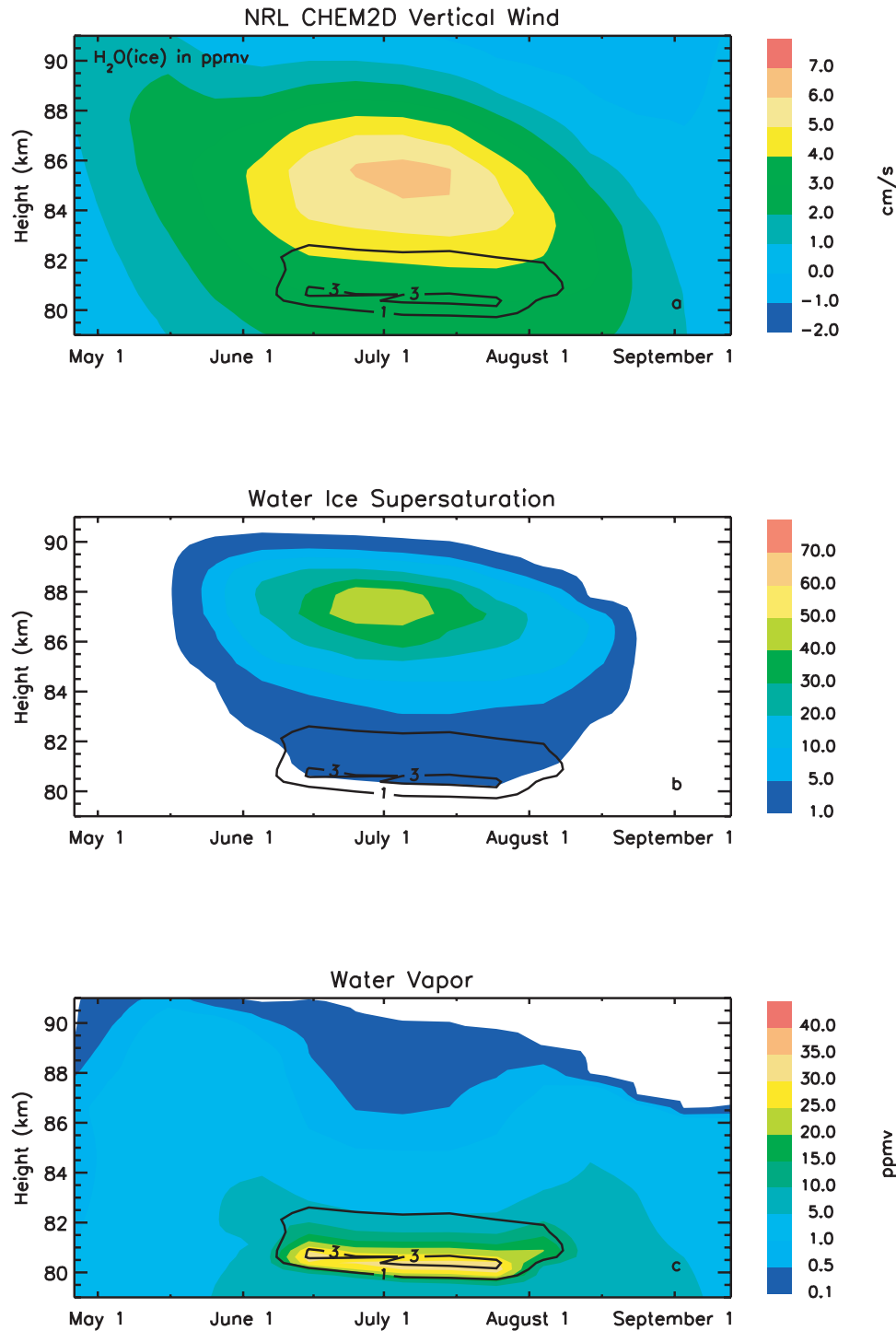


Figure 7. (a) Seasonal variation of vertical winds in the Arctic summer mesosphere (71°N). Winds are from a two-dimensional photochemical/dynamical model [Siskind *et al.*, 2005] and are used as input to the CARMA microphysical model. Equivalent water vapor, $H_2O(ice)$, is overplotted as black contours in ppmv. (b) Water ice supersaturation ($S > 1$) calculated from temperatures and water vapor. (c) Vertical and seasonal distribution of water vapor in the Arctic summer mesosphere. The observed HALOE water vapor is redistributed vertically through ice formation, sedimentation, and sublimation of particles throughout the PMC season.

without regard to PMC frequency, which is far less at the beginning and end of the season than in the middle. To better represent the PMC ice mass, we multiply the long-dashed line by the HALOE PMC occurrence frequency

during the same time period. This result is shown as the short-dashed line in Figure 8.

[41] As with any set of PMC observations, the HALOE data have a detection threshold so that clouds with weaker

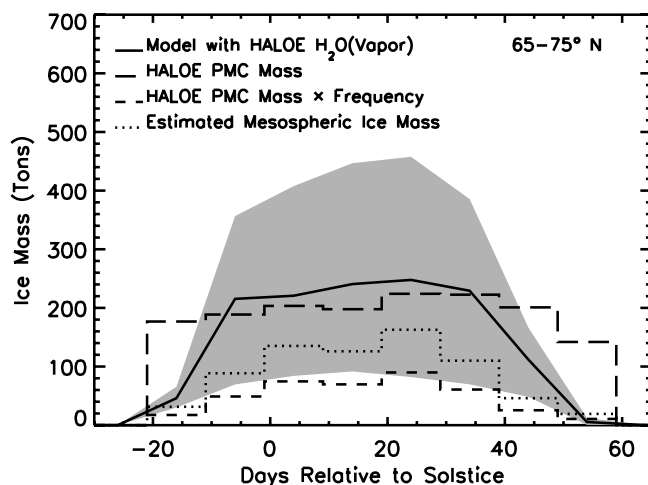


Figure 8. Ice mass in the Arctic mesosphere. The shaded area represents the minimum and maximum amount of ice forming during each 4-day model simulation. The long-dashed line is based on reported HALOE $\text{H}_2\text{O}(\text{ice})$ observations, and the short-dashed line is the result of multiplying this ice mass with the HALOE observation frequency. The dotted line includes an estimation for the subvisible PMCs (see Figure 9).

signals are missed. These weaker clouds may be abundant and may contribute substantially to the total mesospheric ice mass. To properly compare the HALOE data with our model results in Figure 8, we therefore now estimate this contribution in Figure 9. Figure 9a shows the cumulative number of observed clouds between -16 and 54 DRS that have a larger peak extinction (β) at $3.40 \mu\text{m}$ than the value on the x axis. This is analogous to the g distribution sometimes employed for observations of solar scattered light in the UV [Thomas, 1995; DeLand et al., 2003]. The advantage of the HALOE PMC extinction measurements, however, is that they are linearly related to ice volume density [Hervig et al., 2003] and are independent of the ice particle size distribution. Note that the local times for the data in Figure 9 generally range between 23.9 and 0.7 local time and so are biased to late night conditions.

[42] We have no direct information on the behavior of the curve in Figure 9a for small extinctions. However, since the normalized cumulative frequency in Figure 9a cannot exceed unity and the slope of the data suggests that the y intercept could be at or near unity for small extinctions, we extrapolate Figure 9a to one for zero extinction and show this extrapolation as the dashed line. By doing this, we are assuming that some ice particles always exist (but are not always detected) for the conditions indicated.

[43] Figure 9b shows the distribution of peak β values using the extrapolated curve in Figure 9a so that the integral of the frequencies over β is unity. Since the extinction is linearly related to ice volume density and therefore ice mass, relative cloud extinction and relative cloud mass are synonymous. By multiplying each β by its corresponding frequency in Figure 9b, we find the relative contribution to the mesospheric ice mass from each β , and this is shown in Figure 9c. As indicated in Figure 9c, we estimate that the PMC mass is 55% of the total mesospheric ice mass.

[44] We therefore multiply the observations in Figure 8 (short-dashed line) by a factor of 1.8 to estimate the total mesospheric ice mass from HALOE PMC observations, and this result is shown as the dotted line, which we compare directly to the model. From the dotted line in Figure 8, 90 ± 12 t of ice are present between 65° and 75°N when averaged over the PMC season (-16 to -54 DRS). The 14% uncertainty is a root sum square of the measurement uncertainty in β (8%), the conversion of the extinction to the ice volume (5%), and the neutral air density (10%) [McHugh et al., 2003; Hervig et al., 2003]. The average mesospheric ice mass is still a factor of 1.8 smaller than the average CARMA result in Figure 8 of 165 t but within the time-dependent variability of the model result shown by the shaded area. The model result is also subject to uncertainties in the prescribed temperature, water vapor, and vertical winds, and these will be discussed further in section 4.

[45] Direct comparison of the HALOE PMC ice mass in Figure 8 obtained near midnight and the SBUV PMC ice mass in Figure 5 obtained near 4.7 local time is tempting but unreliable since we currently have limited data on the diurnal variation of the water vapor and the water ice mass near 82 km in the Arctic summer [von Zahn et al., 1998]. Model results suggest that the directional albedo of PMCs can vary by more than a factor of 3 over a day so that care must be taken when comparing the PMC ice mass at different local times [Jensen et al., 1989]. Furthermore, solar cycle effects on the PMC frequency can exceed a factor of 4 [DeLand et al., 2003] so that a comparison of the

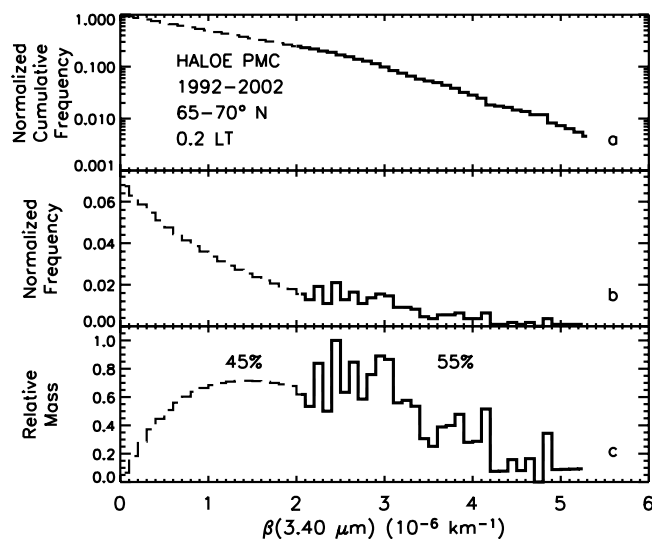


Figure 9. (a) Normalized cumulative frequency of the HALOE peak cloud extinctions at $3.40 \mu\text{m}$ (solid line) for the conditions shown. The data have been extrapolated to unity for zero extinction (dashed line). The HALOE detection threshold is $2 \times 10^{-6} \text{ km}^{-1}$. (b) Normalized frequency of the HALOE PMC data for the curve in Figure 9a. The integral under the all normalized frequencies is unity. (c) Relative contribution to the mesospheric ice mass from all peak cloud extinctions. The contribution from the observations is 55%, and the estimated contribution from the clouds below the HALOE detection threshold is 45%.

Table 1. Sensitivity of Predicted Ice Mass to Inputs^a

	Input Uncertainty	Effect on Ice Mass, ^b %
Vertical wind	±50%	±40
Temperature	±5 K	±40
Water vapor	±18%	±20

^aConditions for day of year 186.^bTime average between 24 and 96 hours of cloud growth and sublimation.

SBUV ice mass averaged over one season with the HALOE ice mass inferred over a solar cycle could be misleading.

4. Discussion

4.1. On the Shuttle and Launch Vehicle Contribution

[46] Our conclusion that PMCs formed from shuttle exhaust are 22% of the PMC ice mass between 65° and 75°N indicates that even one shuttle launch can be important in a season of PMC observations. So far, there is strong evidence of two separate northern summer shuttle plumes reaching the Arctic to form PMCs (STS 85 and STS 93). Although reported summertime mean meridional winds near 110 km are northward [Wang *et al.*, 1997], it is not known whether every northern summer shuttle plume finds its way to the Arctic to form PMCs in the same way. We nonetheless consider the implications of that possibility now.

[47] We can estimate the PMC contribution based on the shuttle launch frequency and our estimated ice mass. From 1992 to 2002, there were on average 1.3 shuttle launches during the PMC season which we define to be 31 May to 19 August. This means that if each of those shuttle plumes reached the Arctic, the total contribution would be 29% between 65° and 75°N based on our analysis of the STS 93 shuttle plume contribution shown in Figure 5. We regard this as an upper limit because a cursory look at SBUV data from other years in general does not reveal as much of a response as shown in Figure 5.

[48] An additional contribution would also come from the more numerous but smaller launch vehicles worldwide. On average, there were 15 launches of smaller vehicles each PMC season for the same 1992–2002 time period. Using the amount of fuel in the appropriate stage for each vehicle, the flight path and the water yield for each propellant combination we estimate on average another 100–200 t of water every PMC season injected between 90 and 140 km [Simmons, 2000; Isakowitz *et al.*, 1999; American Institute of Aeronautics and Astronautics, 1991]. This is 20–40% of the total water coming from shuttles over the same altitudes during the northern PMC season and raises the potential contribution from rockets to 35–40%. We note that a shuttle plume is not readily destroyed and can retain ~60–180 t of water even after 4 days [Stevens *et al.*, 2003]. We therefore cannot rule out additional contributions to the season of SBUV PMC observations from other launch vehicle plumes injected before June.

[49] A cause and effect study of launch vehicle plumes forming PMCs is currently hampered by limited synoptic water vapor observations above 90 km and an incomplete understanding of plume transport in this region of the atmosphere. In particular, mean meridional winds between

90 and 140 km as inferred from plume transport are much faster than what is typically reported from climatologies or general circulation models [Stevens *et al.*, 2002, 2003; Siskind *et al.*, 2003]. Results from chemical release experiments, however, consistently show remarkably strong winds between 100 and 110 km with large shears [Larsen, 2002]. Significant insight could be gained by additional plume observations to help justify their large-scale motion with existing models and wind observations.

4.2. Model-Data Discrepancies in Mesospheric Ice Mass

[50] The observed beginning and end of the PMC season is reproduced well by the one-dimensional CARMA model. However, as shown in Figure 8, CARMA overpredicts the peak ice mass of the Arctic summer mesosphere by a factor of 1.8 compared to the mesospheric ice mass inferred from HALOE observations. This is noteworthy because the model is initialized with water vapor observations made with the same satellite experiment. We compare the sensitivity of the ice mass to quoted or estimated uncertainties in water vapor and other key inputs in Table 1. Uncertainties for vertical winds are estimated to be 50% based on the range of values reported for the Arctic summer mesosphere [Körner and Sonnemann, 2001; Berger and von Zahn, 2002; Siskind *et al.*, 2005]. Temperature uncertainties (±5 K) are interpolated to 85 km from Lübken [1999]. Water vapor uncertainties (±18%) are calculated from the root sum square of the uncertainties reported by McHugh *et al.* [2003]. For each test case listed, the entire input vertical profile was uniformly adjusted by the amount indicated to estimate the resultant effect on the ice mass, which was rounded to the nearest 10%. The results in Table 1 yield a root-sum-square total of ±60% uncertainty in the ice mass due to the model input parameters.

[51] Given the sensitivity of the absolute ice mass to model inputs and the excursions in the mass resulting from the natural competition between upwelling and ice particle sedimentation (Figures 6 and 8) we do not regard the factor of 1.8 overprediction of the HALOE ice mass as severely discrepant with the data, particularly given the omission of local time effects on the modeling approach. The shape of the model in Figure 8 nonetheless serves as an important guide to establishing a baseline in Figure 5 from which to infer the contribution of shuttle PMCs.

5. Summary

[52] We find that PMCs formed from the water exhaust of one space shuttle launch accounts for 22% of all PMC ice mass measured by SBUV near 4.7 LT in 1999 between 65° and 75°N. This is the first indication that shuttle PMCs can help drive the observed week-to-week PMC variability. We therefore caution that some features present in PMC data sets may not be due to large-scale dynamical effects at 82 km but rather to a fluctuating water source from above. The SBUV PMC data consist of observations from every summer back to 1979 for both hemispheres and include the entire flight history of the shuttle program. Analysis of this data in the manner described herein is underway.

[53] Using reprocessed HALOE water vapor observations from the Arctic summer mesosphere in a one-dimensional microphysical model, we have predicted the mesospheric ice mass. The model produces an average of 165 t of ice between 65° and 75°N, which is a factor of 1.8 greater than that inferred from simultaneous HALOE observations (90 ± 12 t). Due to the time-dependent variability of ice formation and the uncertainty of vertical winds, temperature, and water vapor, this is reasonably consistent with model results.

[54] The use of the ice mass as a measure of Arctic PMCs has allowed us to quantify the shuttle contribution to the cloud season and facilitated a comparison of PMC data with microphysical model results. Since the ice mass is a measure of both the cloud frequency and brightness (or extinction) we regard this quantity as a useful measure of both short- and long-term changes in the summer polar mesosphere.

[55] **Acknowledgments.** We thank M. Rapp for assistance with the CARMA model and D. E. Siskind for providing us with results from NRL's CHEM2D model. This work was supported by the Office of Naval Research and the NASA Office of Space Science.

[56] Arthur Richmond thanks Xinzhaoh Chu and another reviewer for their assistance in evaluating this paper.

References

- American Institute of Aeronautics and Astronautics (1991), *Atmospheric Effects of Chemical Rocket Propulsion*, 52 pp., Am. Inst. of Aeronaut. and Astronaut., New York.
- Berger, U., and U. von Zahn (2002), Icy particles in the summer mesopause region: Three-dimensional modeling of their environment and two-dimensional modeling of their transport, *J. Geophys. Res.*, **107**(A11), 1366, doi:10.1029/2001JA000316.
- Bohren, C. F., and D. R. Huffman (1983), *Absorption and Scattering of Light by Small Particles*, Wiley-Interscience, Hoboken, N. J.
- Debresterian, D. J., et al. (1997), An analysis of POAM II solar occultation observations of polar mesospheric clouds in the Southern Hemisphere, *J. Geophys. Res.*, **102**(D2), 1971–1981.
- DeLand, M. T., E. P. Shettle, G. E. Thomas, and J. J. Olivero (2003), Solar backscattered ultraviolet (SBUV) observations of polar mesospheric clouds (PMCs) over two solar cycles, *J. Geophys. Res.*, **108**(D8), 8445, doi:10.1029/2002JD002398.
- Donahue, T. M., B. Guenther, and J. E. Blamont (1972), Noctilucent clouds in daytime: Circumpolar particulate layers near the summer mesopause, *J. Atmos. Sci.*, **36**, 515–517.
- Fiedler, J., G. Baumgarten, and G. von Cossart (2003), Noctilucent clouds above ALOMAR between 1997 and 2001: Occurrence and properties, *J. Geophys. Res.*, **108**(D8), 8453, doi:10.1029/2002JD002419.
- Gadsden, M. (1982), Noctilucent clouds, *Space Sci. Rev.*, **33**, 279–334.
- Hartogh, P., and L. Song (2004), Microwave detection of rocket exhaust plumes in the lower thermosphere, paper presented at the First International Conference on Submillimeter Science and Technology, Phys. Res. Lab., Ahmedabad, India, October 13–15.
- Hervig, M., et al. (2001), First confirmation that water ice is the primary component of polar mesospheric clouds, *Geophys. Res. Lett.*, **28**(6), 971–974.
- Hervig, M., M. McHugh, and M. E. Summers (2003), Water vapor enhancement in the polar summer mesosphere and its relationship to polar mesospheric clouds, *Geophys. Res. Lett.*, **30**(20), 2041, doi:10.1029/2003GL018089.
- Isakowitz, S. J., J. P. Hopkins, and J. B. Hopkins (1999), *International Reference Guide to Space Launch Systems*, 3rd ed., Am. Inst. of Aeronaut. and Astronaut., Reston, Va.
- Jensen, E. J., and G. E. Thomas (1988), A growth-sedimentation model of polar mesospheric clouds: Comparisons with SME measurements, *J. Geophys. Res.*, **93**(D3), 2461–2473.
- Jensen, E., G. E. Thomas, and O. B. Toon (1989), On the diurnal variation of noctilucent clouds, *J. Geophys. Res.*, **94**(D12), 14,693–14,702.
- Kirkwood, S., and K. Stebel (2003), Influence of planetary waves on noctilucent cloud occurrence over NW Europe, *J. Geophys. Res.*, **108**(D8), 8440, doi:10.1029/2002JD002356.
- Körner, U., and G. R. Sonnemann (2001), Global three-dimensional modeling of the water vapor concentration of the mesosphere-mesopause region and implications with respect to the noctilucent cloud region, *J. Geophys. Res.*, **106**(D9), 9639–9651.
- Larsen, M. F. (2002), Wind and shears in the mesosphere and lower thermosphere: Results from four decades of chemical release wind measurements, *J. Geophys. Res.*, **107**(A8), 1215, doi:10.1029/2001JA000218.
- Leslie, R. (1885), Sky glows (abstract), *Nature*, **32**, 245.
- Lieberman, R. S., et al. (2000), Comparison of mesospheric and lower thermospheric residual wind with High Resolution Doppler Imager, medium frequency, and meteor radar winds, *J. Geophys. Res.*, **105**(D22), 27,023–27,035.
- Lübken, F.-J. (1999), Thermal structure near the Arctic mesopause in summer, *J. Geophys. Res.*, **104**(D8), 9135–9149.
- Mauersberger, K., and D. Krankowsky (2003), Vapor pressure above ice at temperatures below 170 K, *Geophys. Res. Lett.*, **30**(3), 1121, doi:10.1029/2002GL016183.
- McHugh, M., M. Hervig, B. Magill, R. E. Thompson, E. Remsberg, J. Wrotny, and J. M. Russell III (2003), Improved mesospheric temperature, water vapor and polar mesospheric cloud extinctions from HALOE, *Geophys. Res. Lett.*, **30**(8), 1440, doi:10.1029/2002GL016859.
- Rapp, M., F.-J. Lübken, A. Müllemann, G. E. Thomas, and E. J. Jensen (2002), Small-scale temperature variations in the vicinity of NLC: Experimental and model results, *J. Geophys. Res.*, **107**(D19), 4392, doi:10.1029/2001JD001241.
- Simmons, F. S. (2000), *Rocket Exhaust Plume Phenomenology*, Aerospace Press, El Segundo, Calif.
- Siskind, D. E., et al. (2003), Signatures of shuttle and rocket exhaust plumes in TIMED/SABER radiance data, *Geophys. Res. Lett.*, **30**(15), 1819, doi:10.1029/2003GL017627.
- Siskind, D. E., M. H. Stevens, and C. R. Englert (2005), A model study of global variability in mesospheric cloudiness, *J. Atmos. Sol. Terr. Phys.*, in press.
- Stevens, M. H., et al. (2001), PMCs and the water frost point in the Arctic summer mesosphere, *Geophys. Res. Lett.*, **28**(23), 4449–4452.
- Stevens, M. H., C. R. Englert, and J. Gumbel (2002), OH observations of space shuttle exhaust, *Geophys. Res. Lett.*, **29**(10), 1378, doi:10.1029/2002GL015079.
- Stevens, M. H., J. Gumbel, C. R. Englert, K. U. Grossmann, M. Rapp, and Paul Hartogh (2003), Polar mesospheric clouds formed from space shuttle exhaust, *Geophys. Res. Lett.*, **30**(10), 1546, doi:10.1029/2003GL017249.
- Summers, M. E., et al. (2001), Discovery of a water vapor layer in the Arctic summer mesosphere: Implications for polar mesospheric clouds, *Geophys. Res. Lett.*, **28**(18), 3601–3604.
- Thomas, G. E. (1991), Mesospheric clouds and the physics of the mesopause region, *Rev. Geophys.*, **29**, 553–575.
- Thomas, G. E. (1995), Climatology of polar mesospheric clouds: Interannual variability and implications for long-term trends, in *The Upper Mesosphere and Lower Thermosphere: A Review of Experiment and Theory*, vol. 87, edited by R. M. Johnson and T. L. Killeen, pp. 185–200, AGU, Washington, D. C.
- Thomas, G. E., and C. P. McKay (1985), On the mean particle size and water content of polar mesospheric clouds, *Planet. Space Sci.*, **33**(10), 1209–1224.
- Thomas, G. E., and J. J. Olivero (1989), Climatology of polar mesospheric clouds: 2. Further analysis of Solar Mesosphere Explorer data, *J. Geophys. Res.*, **94**(D12), 14,673–14,681.
- Thomas, G. E., and J. J. Olivero (2001), Noctilucent clouds as possible indicators of global change in the mesosphere, *Adv. Space Res.*, **28**(7), 937–946.
- Thomas, G. E., J. J. Olivero, E. J. Jensen, W. Schröder, and O. B. Toon (1989), Relation between increasing methane and the presence of ice at the mesopause, *Nature*, **338**, 490–492.
- Thomas, G. E., R. D. McPeters, and E. J. Jensen (1991), Satellite observations of polar mesospheric clouds by the Solar Backscattered Ultraviolet Spectral Radiometer: Evidence of a solar cycle dependence, *J. Geophys. Res.*, **96**(D1), 927–939.
- Thomas, G. E., J. J. Olivero, M. DeLand, and E. P. Shettle (2003), Comment on “Are noctilucent clouds truly a ‘miner’s canary’ for global change?” (abstract), *Eos Trans. AGU*, **84**(36), 352.
- Turco, R. P., O. B. Toon, R. C. Whitten, R. G. Keese, and D. Hollenbach (1982), A study of mesospheric rocket contrails and clouds produced by liquid-fueled rockets, *Space Sol. Power Rev.*, **3**, 223–234.
- von Cossart, G., J. Fiedler, and U. von Zahn (1999), Size distributions of NLC particles as determined from 3-color observations of NLC by ground-based lidar, *Geophys. Res. Lett.*, **26**(11), 1513–1516.

- von Zahn, U. (2003), Are noctilucent clouds truly a ‘miner’s canary’ for global change? (abstract), *Eos Trans. AGU*, 84(28), 261.
- von Zahn, U., G. von Cossart, J. Fiedler, and D. Rees (1998), Tidal variations of noctilucent clouds measured at 69°N latitude by ground-based lidar, *Geophys. Res. Lett.*, 25(9), 1289–1292.
- von Zahn, U., U. Berger, J. Fiedler, and P. Hartogh (2004), Noctilucent clouds and the mesospheric water vapour: The past decade, *Atmos. Chem. Phys.*, 4, 2449–2464.
- Wang, D. Y., et al. (1997), Empirical model of 90–120 km horizontal winds from wind-imaging interferometer green line measurements in 1992–1993, *J. Geophys. Res.*, 102(D6), 6729–6745.
- Warren, S. G. (1984), Optical constants of ice from the ultraviolet to the microwave, *Appl. Opt.*, 23(8), 1206–1225.
-
- M. T. DeLand, Science Systems and Applications, Inc., 10210 Greenbelt Rd., Suite 400, Lanham, MD 20706, USA.
- C. R. Englert and M. H. Stevens, E.O. Hulburt Center for Space Research, Naval Research Laboratory, 4555 Overlook Ave. SW, Code 7641, Washington, DC 20375-5320, USA. (stevens@uap2.nrl.navy.mil)
- M. Hervig, GATS, Inc., 65 South Main, #5, Driggs, ID 83422, USA.